Originals

Experiments in Fluids 23 (1997) 1–13 © Springer-Verlag 1997

Experimental study of coating flows in a partially-filled horizontally rotating cylinder

S. T. Thoroddsen, L. Mahadevan

Abstract We describe a number of different phenomena seen in the free-surface flow inside a partially filled circular cylinder which is rotated about its horizontal axis of symmetry. At low angular velocities the flow settles into a steady two-dimensional flow with a front where the coating film coalesces with the pool at the bottom of the cylinder. This mode becomes unstable at higher angular velocities, initially to a sloshing mode on the rising side of the coating film and then to an axial instability on the front. The undulations that appear on the front grow into large-amplitude stationary patterns with cusp-like features for some parameter values. At still higher angular velocities and volume fractions, a number of different inertial instabilities and patterns appear. We present a phase diagram of the various transitions and characterize some of the more prominent instabilities and patterns in detail, along with some possible mechanisms for the observed behaviour.

1 Introduction

Coating flows are fluid flows which lead to thin films of liquid forming onto surfaces as a result of external forces associated with inertia, viscosity, gravity, surface tension etc. Besides being important in a number of industrial processes, Benkreira et al. (1994), they form an interesting system in which to study free-surface instabilities in hydrodynamics.

In this paper, we present some experimental observations of the behaviour of a viscous fluid partially filling a horizontally rotating cylinder. We undertake a comprehensive experimental study of the various phenomena that present themselves in the course of the transition from the stationary pool at the bottom of the cylinder to the homogeneous rimming flow uniformly coating the cylinder, for various values of the problem parameters. Our main aim is to present a reasonably complete catalog of the various phenomena observed, including some that seem to have escaped the attention of earlier researchers.

The system is atypical, in that although the extreme states of the fluid flow corresponding to angular velocities of zero and infinity are trivial, a complicated sequence of transitions connects these two states. At zero velocity, the fluid is stationary and lies in a pool at the bottom of the cylinder, while at very high angular velocity, the fluid rotates rigidly with the cylinder and forms a homogeneous film that coats the cylinder uniformly. It might not be an exaggeration to suggest that this configuration is the free-surface analog of the well-studied Taylor–Couette problem.

An early study of free-surface flows in this geometry goes back to the work of Balmer (1970), who pointed out the existence of hygrocysts, or walls of water in rapidly rotating partially filled horizontal cylinders. Kovac and Balmer (1980) have also studied external hygrocysts experimentally. Later Karweit and Corrsin (1975) documented similar observations but without quantifying them. Phillips (1960) analyzed the propagation of disturbances on the free surface of the homogeneous fluid film that coats the cylinder at large angular velocities, while Ruschak and Scriven (1976), Orr and Scriven (1978) and Lin (1986) studied the two-dimensional problem numerically and observed recirculation zones in the flow. All these studies took viscosity, surface tension and inertia into account.

In 1977, Moffatt used lubrication theory to study the problem of a viscous film coating the exterior of a cylinder. Following earlier ideas of Lighthill and Whitham, he presented a kinematic wave model to partially explain the evolution of perturbations in the azimuthal direction, that lead to backward-breaking waves. He also presented some qualitative experiments that suggested a large number of questions that remain unanswered.

Later work inspired by Moffatt's paper includes the papers of Johnson (1988), Preziosi and Joseph (1988), Melo (1993) and most recently Benjamin et al. (1995) and Goodwin and Tavener (1996). These authors have focused on trying to achieve an analytical and numerical understanding of the steady two-dimensional coating flow at low angular velocities which shows a singularity that is regularized by surface tension. Melo (1993) presented some experimental data for the onset of

Received: *13 April 1996*/*Accepted*: *13 June 1996*

S. T. Thoroddsen, L. Mahadevan[1]
Department of Theoretical and Applied Mechanics,
University of Illinois at Urbana-Champaign
Urbana, iL 61801-2935, USA

[1] *Current address*: Mechanics and Materials, Room 1-310, M.I.T., 77 Mass. Ave., Cambridge, MA 02139, USA

Correspondence to: S. T. Thoroddsen

The initial impetus for this study was provided by the preliminary investigations of Chris Lawrence and Hong-Biao Zhang, see Zhang (1995). We thank them for getting us interested in the experiment. We acknowledge discussions with Simon Tavener, Ralph Goodwin, Michael Brenner, Nigel Goldenfeld, Ronald Adrian and Robert Johnson. We also thank Hassan Aref for his continued encouragement of this work. STT is supported by the University of Illinois Research Board.

three-dimensional instabilities followed by some analysis based on Moffatt's lubrication theory. Other attempts at determining the wavelength of the spanwise undulations (Johnson 1990; Zhang 1995) have not been successful. Vallette et al. (1994) have studied the spatio-temporal chaos in the waves on the front.

Before continuing, we mention two widely studied configurations that are related to the current experiment, and shed some light on the possible mechanisms of instability and pattern formation. The first is the classic experiment of flow of a thin fluid film down an inclined plane, first studied by Kapitza and Kapitsa (1949) and recently by Goodwin and Homsy (1991) who give a summary of the history of the problem. The ridge of fluid at the contact line in this configuration becomes unstable to height perturbations in the transverse direction and leads to the evolution of finger-like patterns that evolve with time, which are only just beginning to be understood theoretically. We will argue later that the axial instability in our experiment may arise for related reasons, although their evolution is very different.

A second related configuration arises in the flow between two eccentrically mounted rotating cylinders separated by a small gap. This setup was first studied by Pearson (1960) and recently has been the subject of a series of papers by Rabaud et al. (1991) and Rabaud (1994), and Pan and deBruyn (1994) and deBruyn and Pan (1995) where variety of stationary patterns, traveling waves and their stability, and spatio-temporal chaos have been reported on. An essential difference between this configuration and ours is that the free-surface in the so-called printer's instability is essentially one-dimensional, which is clearly not the case in the coating flow problem.

In Sect. 2, we present the various dimensionless numbers that govern this phenomenon. In Sect. 3 we describe the experimental setup. Experimental results are presented in Sect. 4 and correspond to observations of the free-surface flow as the angular velocity, volume fraction and viscosity of the fluid are varied.

2
Dimensionless parameters

The richness of flow phenomena observed here arises due to the interaction of gravity, viscous forces, inertial forces as well as surface tension. To quantify the dependence of the various transitions in the coating flow on these forces, we resort to dimensional analysis. The various problem parameters are: the radius R, and length ℓ of the cylinder, the volume of fluid V_f, the density ρ, the viscosity μ and the surface tension σ, the angular velocity of the cylinder ω and the acceleration of gravity g. Therefore, by the Buckingham π theorem, there are 5 dimensionless numbers, say

$$Re = \rho\omega R h_0/\mu, \quad Fr = \omega^2 R/g \tag{2.1}$$

$$Ca = \mu\omega R/\sigma, \quad A = \ell/R$$

$$\eta = V_f/(\pi R^2 \ell)$$

Here $h_0 = V_f/(2\pi R\ell)$ is the mean film thickness, Re is the Reynolds number based on this thickness and the cylinder velocity, Fr is the Froude number, Ca is the capillary number and A is the aspect ratio of the cylinder. The volume filling fraction is denoted by η. We note that the Reynolds number as defined represents the ratio of the inertial to the viscous forces only when there is a pool at the bottom of the cylinder so that there is a velocity gradient inside the fluid. At large enough angular velocities, the fluid moves rigidly along with the boundary and there is no relative motion and the effective Reynolds number is zero.

The experiments are conducted over a wide range of these parameters. The Reynolds numbers ranged from 10 to 20000 (based on Eq. (2.1)). Most of the phenomena are observed for capillary numbers in the range from about 2 to 120.

3
Experimental setup

The experimental apparatus is a modification of a previous device built by Johnson (1988) and later used by Zhang (1995). It consists of a circular plexiglass cylinder supported at the ends by two conical shafts. The drive-shaft is keyed to a pulley and is connected to the motor through interchangeable wheels driven by a belt. Two separate motors were used during these experiments. Both had a speed range of 1750 rpm, with manual speed control and a least-count of 0.5% of the maximum. This allowed cylinder angular velocities of up to 8 cylces/s. The angular velocity was determined directly by measuring the time required for a specific number of rotations of the cylinder using a stopwatch and comparison with a calibrated tachometer. Repeated calibrations showed that the tachometer agreed with the direct measurements to within 0.5%. Investigations of video frames shows that long term variation in the rotation rate is negligible. The observed flow phenomena were independent of the direction of rotation. The cylinder axis was levelled using the fluid level inside the stationary cylinder. The coordinate axes and important dimensions are defined in Fig. 1. The fluid viscosity was varied by more than two orders of magnitude by using a glycerin-water mixture of varying concentration, giving values between 2 and 1020 centipoise. The density of the mixture increases somewhat with the viscosity, as the specific gravity of the glycerin was 1.22. The surface tension was measured using a ring-tensiometer and was observed to be fairly independent of the mixture strength, being about 69 ± 4 dyn/cm. Care was taken to ensure that hygroscopic effects were not important. The viscosity of the mixture was frequently measured and the room temperature was monitored. The fluid was dyed with Congo Red dye to facilitate visualization.

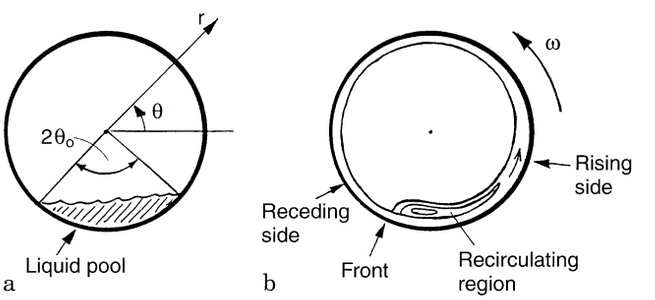

Fig. 1a, b. Schematic of the cylinder cross-section and the coordinate system. **a** The liquid pool at the bottom of the cylinder spanning angle $2\theta_0$ at rest; **b** formation of the front on the receding side of the cylinder, during rotation

The results discussed here were primarily obtained with a cylinder of inside-radius $R = 6.25$ cm and aspect ratio ℓ/R of 7.8. Unless otherwise stated, we always refer to the results obtained using this cylinder. Four other cylinders were used in specific cases. They had the following inner radii and (aspect ratios): 2.35 cm (16.0), 3.8 cm (15.4), 7.1 cm (8.2) and 14.6 cm (5.9). The aspect ratios were based simply on the ease of availability of the cylinders.

The volume filling fraction η was varied between 1% and about 30%. Dewetting of some parts of the surface did sometimes occur for very small volume fractions, but was avoided in the experiments and limited the smallest volume fractions that could be studied. Care was taken to adjust the angular velocity slowly (compared to the viscous time scale) and in small increments, and to let the flow adjust to the new conditions, as will be described in Sect. 4.4.1.

4
Experimental results

4.1
General flow phenomena

We start by describing a typical progression of phenomena encountered when the angular velocity of the cylinder is increased. Initially the liquid sits in a pool on the cylinder bottom, filling an angle $2\theta_0$, defined in Fig. 1a. At very slow rotation rates a thin film is pulled out of the pool, wetting the entire cylinder inner surface. As the fluid film enters the bottom pool on the receding side a sharp straight front is created. An accompanying recirculation region is also formed in the pool, as shown schematically in Fig. 1b. This recirculating region grows in the azimuthal direction with increasing ω and the front is pulled farther in the θ direction. With increased angular velocity the sheet pulled out of the pool also thickens. It eventually becomes unstable to a sloshing mode of motion on the rising side of the cylinder. This falling wave is initially straight along the span, but at higher ω it breaks up into a number of separate 2-dimensional capillary-gravity waves with approximately parabolic shapes. For a limited range of ω these waves, which we call pendants are stationary. At still larger ω this sloshing instability is overcome by the viscous shear and the flow becomes essentially 2-dimensional. For even higher angular velocity the front on the receding side of the cylinder, where the fluid enters the pool becomes unstable and often develops undulations. The amplitude of these undulations grows with ω and the free surface develops cusp-like features for certain parameter values. At very high angular velocities the front gets pulled over the top of the cylinder. In this rimming mode where centrifugal forces dominate, the fluid coats the cylinder surface uniformly and rotates rigidly with it. The angular velocity ω_u at which the fluid just enters the rimming mode (when ω is increased) is larger than the angular velocity ω_d at which the fluid leaves the rimming mode (when ω is decreased). This hysteresis is more pronounced for larger filling fractions.

Other phenomena associated with the transition regions include the popping or fluttering of surface features associated with strong localized vortical flows inside the sheet, air entrainment at the front, which sometimes leads to frontal avalanches and the shedding of hydroplaning drops. For large filling-fractions curtains or hygrocysts [Balmer, 1970] spanning the entire cross-section of the cylinder are formed. For small fluid viscosity the flow inside the pool and the rising sheet of fluid becomes strongly turbulent. However some patterns do persist even in the presence of this turbulent flow.

Figure 2 shows the regions of parameter space where the different flow phenomena were observed. Each of these figures characterizes the phenomena for a fixed value of viscosity, in terms of ω and η. Notice the overlapping of some of the regions, such as the coexistence of the sloshing instability and counterflowing jets inside the pool, shown in Fig. 2(a).

We next turn to more detailed description of the various phenomena mentioned above.

4.2
Sloshing instability

Initially the thin film pulled out of the pool is stable and the front is straight in the axial direction. As the angular velocity increases, the location of the front gets pulled farther in the direction of the rotation.

A crude measure of the coating capability is given by the angular velocity required to pull the front to the bottom of the cylinder, $\theta = 270^\circ$. The effective angular velocity scales with $\eta^2 g/R\mu$, as is shown in Fig. 3. This scaling is a result of balancing gravity $g \sin\theta h$ and the effective viscous force $\mu\omega R/h$, assuming that for small volume fractions $\eta \approx h/R$. Simultaneously, the film being pulled out of the advancing edge of the pool thickens. At a critical angular velocity ω_c this rising film becomes unstable and it begins to slosh to and fro. The onset of this instability is fairly independent of η for fixed μ, as shown in Fig. 4. Comparison between the results for different values of μ shows that the onset of the instability is delayed with increased viscosity and $\omega_c \sim O(\mu^{1/4})$ as shown in Fig. 5.

The edge of the sloshing film does not remain straight as ω increases and breaks up into a series of falling pendant-like objects (see Fig. 6 below). These pendants are randomly spaced along the cylinder's axis. For even larger ω the pendants get pulled over the top of the cylinder. The angular velocity at which the pendants disappear ω_0 is also shown in Fig. 4. The restabilization occurs in a rather constant band, independent of viscosity. The restabilization shows however a weak, but clear dependence on η, i.e. for larger volume fractions it stabilizes at lower ω, see Fig. 4. The dashed lines in Fig. 4 mark the η-bounds of the unstable region, beyond which no instability was observed.

The evolution of the falling film as ω is increased is not regular and depends strongly on the angular acceleration. This leads to a variety of phenomena: the falling front exhibits axial traveling wave, just before the straight front breaks up into pendants. Frequently, two or more sloshing wave fronts appear at different angular locations in the sheet. This is true for both the less viscous cases, as well as for the largest cylinder. In isolated cases the same edge of the sloshing front splits into two parts, one part falls down as before, while the other part is pulled over the top of the cylinder. Vallette et al. (1994) and Melo and Daoudy (1993) have studied the chaotic behaviour of these travelling waves.

The pendants correspond to capillary gravity waves as shown in Fig. 6 for a stationary isolated pendant. Similarly for randomly falling pendants in this parameter range, intricate

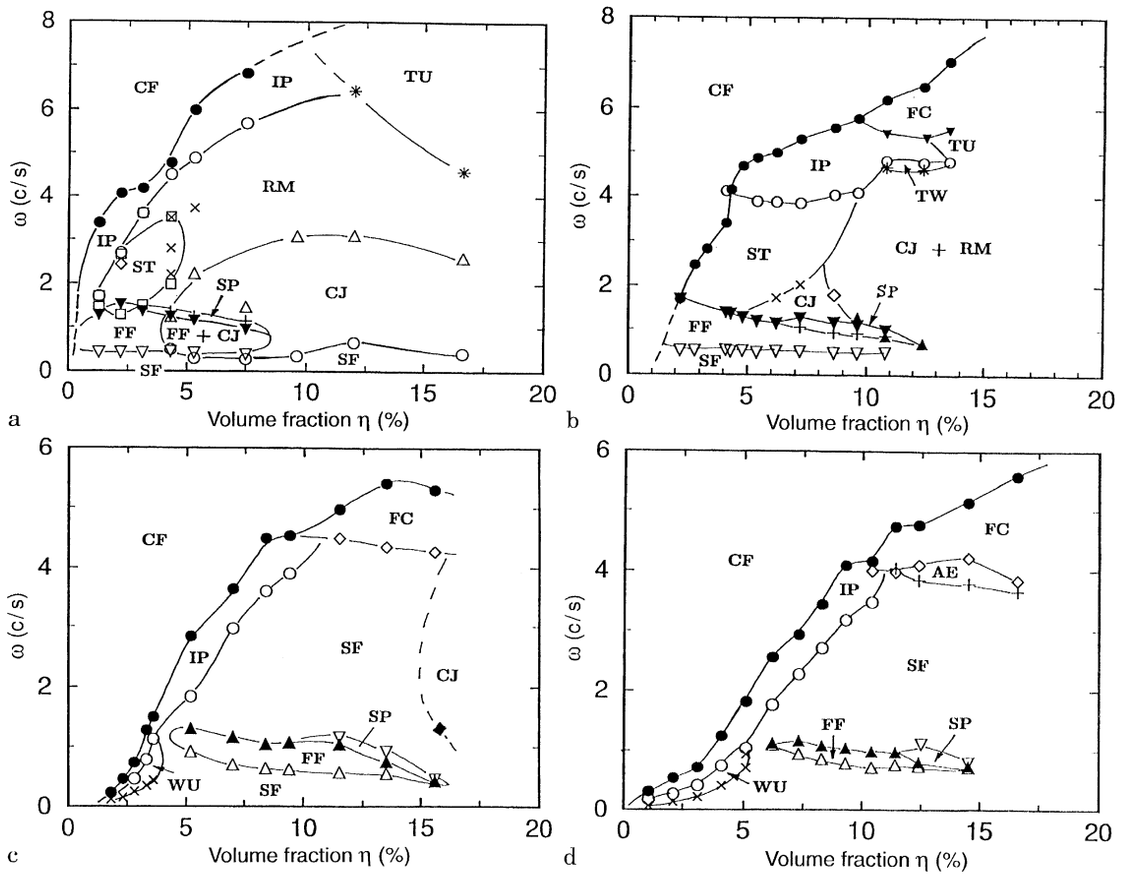

Fig. 2a–d. The classification of flow regimes for fixed viscosity μ and different filling fractions η and rotation rates ω. The states shown are those reached by increasing ω. **a** $\mu = 11$ cP; **b** $\mu = 29$ cP; **c** $\mu = 88$ cP; **d** $\mu = 128$ cP. The initials denote the following flow states: ST = shark teeth; SF = straight stable front; FF = sloshing; SP = stationary pendants; CF = rimming flow; FC = fluid curtains; CJ = counter-flowing jets; AE = air entrainment; TW = traveling waves; IP = incomplete pullover into centrifugal mode; WU = week undulations on the front; TU = turbulence inside the fluid sheet; RM = random motions inside the bottom pool

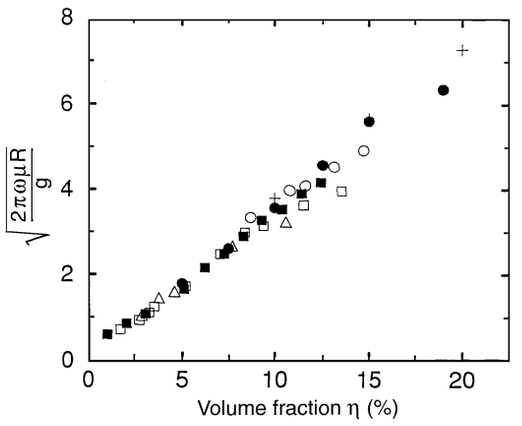

Fig. 3. The effective angular velocities required to pull the front to the bottom of the cylinder, i.e. where $\theta = 270°$, for different η and μ. $\mu = 58$ cP (△); 88 cP (□); 132 cP (■); 144 cP (○); 230 cP (●); 1030 cP (+)

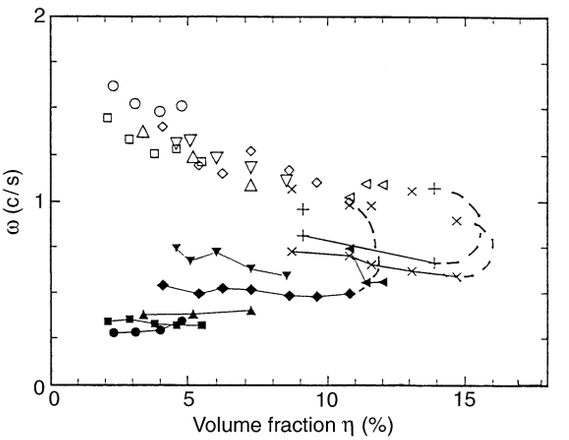

Fig. 4. Parameter range exhibiting the sloshing instability, for different μ. Filled symbols connected with lines show the critical rotation speed where the instability starts. Open symbols denote the rotation speed where the sheet regains stability. Broken lines mark the extent of the regions where this instability is observed, i.e. for larger η no sloshing occurs. Viscosities [cP] are $\mu = 2$ (○); 4 (□); 8 (△); 29 (◇); 68 (▽); 117 (△); 144 (×) and 189 (+)

checkerboard patterns of interacting capillary waves are generated (not shown here). For a more viscous fluid the pendant has only one crest.

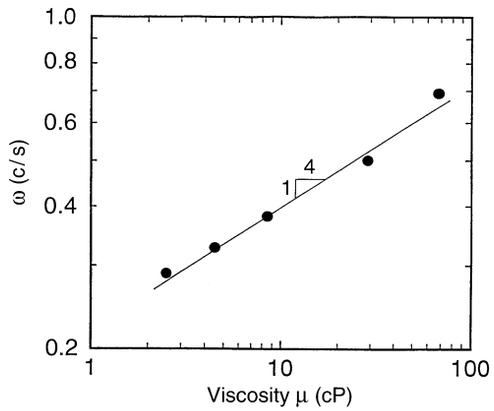

Fig. 5. Onset of the sloshing instability vs viscosity for $\eta \approx 4\%$. The best fit line has a slope of 0.26

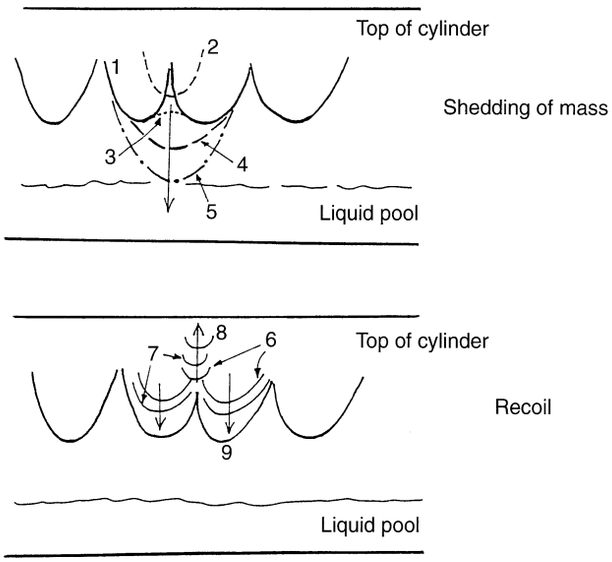

Fig. 8. A sketch made from a sequence of video frames showing the periodic shedding and recovery of fluid between two stationary pendants, for $\mu = 42$ cP and $\eta = 10\%$. The cylinder angular velocity is 1.05 cycles/s and the shedding has a frequency of 0.36 Hz. The times within the shedding cycle are the following, (1) 0.; (2) 0.7; (3) 0.8; (4) 1.0; (5) 1.1; (6) 1.3; (7) 1.5; (8) 1.6; (9) 2.8 sec

4.3
Stationary and oscillating pendants

For a limited range of ω and μ (see Fig. 2) the falling pendants are stationary. This configuration represents a balance between gravity and viscous forces. Figure 6 shows typical shapes of these stationary pendants. The pendants are often align equidistantly along the span, but their formation, as ω is increased, often leaves sections of the cylinder devoid of pendants. For slightly larger ω the viscous stress overcomes gravity and pulls the pendants over the top, leaving a uniform stable sheet. Figure 2 shows the regions of existance of the stationary pendants in the η–ω plane for fixed values of μ. Melo (1993) has reported similar pendants.

A single stationary pendant sometimes appears in a different parameter range at much larger ω, just before the whole straight front is pulled over into rimming mode. In these instances, the straight fluid front is first pulled over into rimming mode at the two ends of the cylinder. With increasing ω this rimming region then progresses towards the center, ultimately leaving an isolated pendant at the center of the cylinder. This pendant is much more pronounced and thicker than the ones described above. Figure 7 shows such a pendant. The curved surface of the cylinder makes the precise determination of the pendant shape difficult, but it is approximately parabolic. The tips of these pendants have higher curvature then the ones describe above. Figure 7 shows the sideview of such a pendant which has induced at strong localized thickening in the fluid sheet above it at the top of the cylinder. At slightly higher ω this thickening ridge will fall through to form a curtain spanning the cross-section, as described in Sect. 4.6.

In a small parameter range, two adjacent stationary pendants sometimes interact dynamically as sketched in Fig. 8 from a sequence of video frames. Excess fluid collects in the region between and above the two pendants and is shed periodically. This fluid falls between the pendants, combining with the two and dragging them down towards the bottom pool. The viscous shear causes them to recoil and the pendants move up on the rising side, where some fluid is transported over the top of the cylinder. The two pendants resume their original positions before the process repeats itself. The mechanism responsible for the oscillations of the pendants is not clear; however they seem to be similar to relaxation oscillations with two time scales.

This mechanism is very stable and the oscillations with a fixed period continue over long times (e.g. it was observed for 900 shedding periods without change).

4.4
Frontal instability and the formation of large amplitude stationary patterns

For an extensive region of parameter space, axial undulations appear on the front on the receding side of the cylinder, see Fig. 1b. These undulations are stable, but sometimes oscillate slightly sideways, especially for smaller viscosities. Figure 9 shows the region in $\mu - \eta$ space where frontal undulations are observed.

The development of the instability with increasing ω is strongly dependent on the volume fraction. For large η the flow-field is dominated by strong counter-flowing jets inside the pool, which can lead to backward-facing (relative to the front) steps resembling duck bills on the pool surface. For smaller η (<6%), the undulations develop large amplitude stationary waves with cusp-like features which we call shark-teeth, characterized by strong vortical flows. Figure 2 shows the regions in $\omega - \eta$ space where the undulations were observed, for different values of μ. For certain values of μ the parameter range where undulations occur can be split up into two regions. The two regions are associated with the above-mentioned shark teeth and duck bills respectively.

The frontal instability and its nonlinear behaviour were observed for all five cylinder sizes tested, representing a variation in cylinder radius by a factor of 6.2. This is evidence that their presence is not limited to a narrow range of cylinder

6

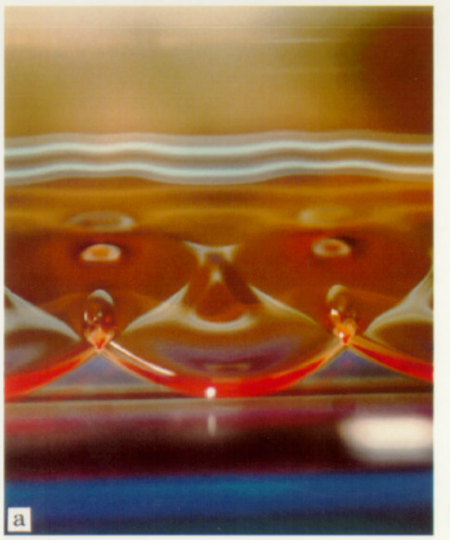

a

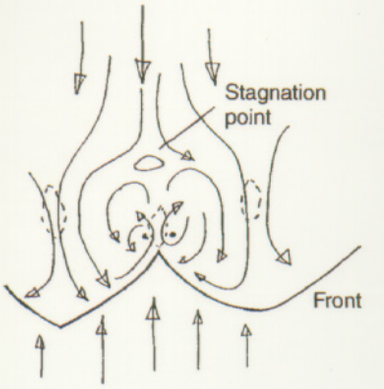

b

14a, b.

7

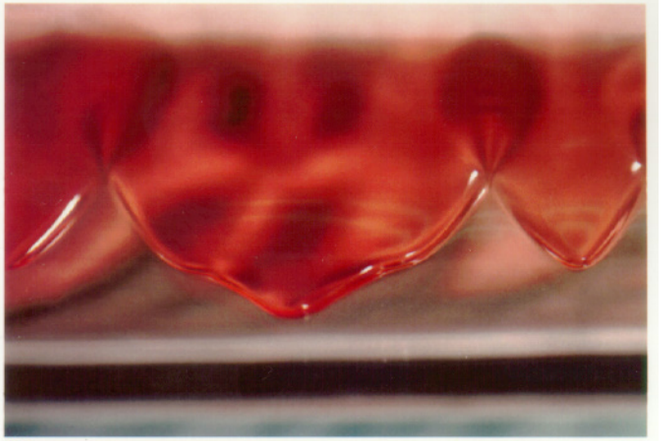

15

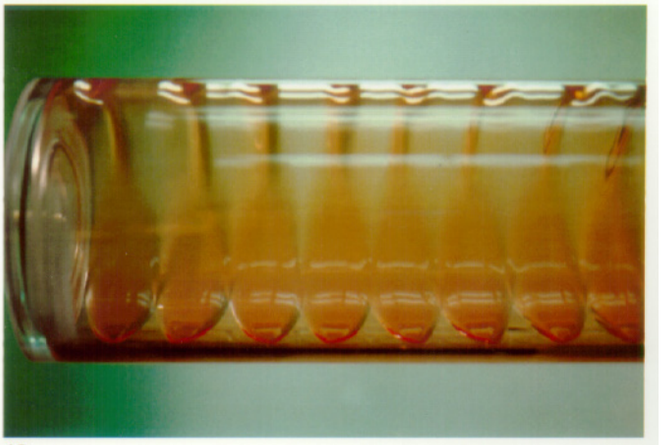

16

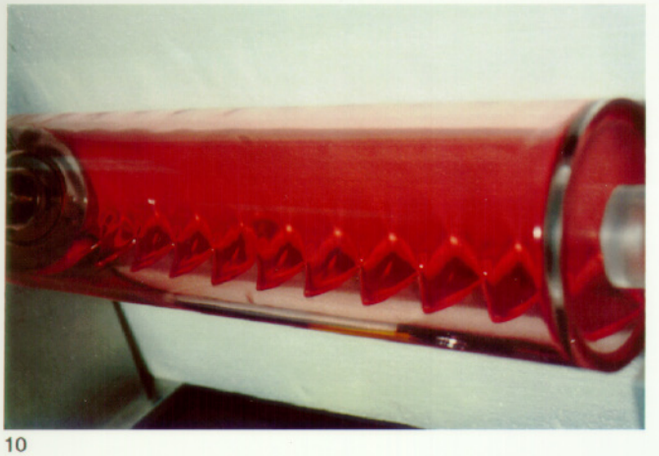

10

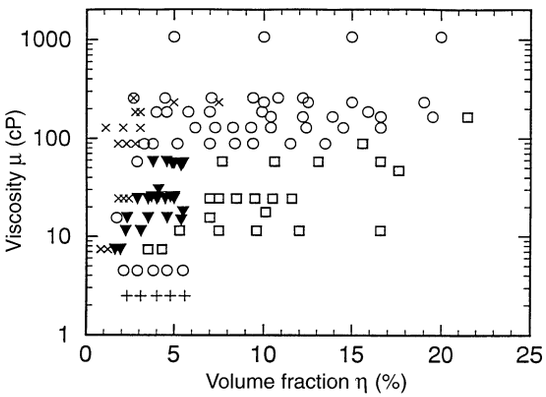

Fig. 9. The regions in μ–η space where frontal undulations were observed for some values of ω. The symbols denote; (○), front remains straight and no undulations form; (▼), shark-tooth-like undulations with cusps; (□), strong counter-flowing jets are set up in the fluid pool, with smooth frontal undulations; (+), clear undulation form on the turbulent front of the pool; (×), week and irregular undulation on the front

curvatures. In fact a similar instability occurs at the contact-line front of a fluid flowing down an inclined plane [Huppert, 1982]. We will now describe each undulation-regime in turn.

4.4.1 Shark-teeth

The frontal undulations start out being approximately sinusoidal, but as ω is increased the amplitude of these undulations grow into cusp-like stationary waves. We call these forms "shark teeth", see Fig. 10.

The changes in wavelength λ and amplitude β of the undulations as a function of ω, were studied for different μ and η. Figure 11 shows typical experimental results for λ vs ω for a fixed μ and a limited range of η. The wavelength λ is not a monotonic function of ω, but appears to be strongly dependent on the angular location of the front. The wavelength λ is a maximum when the front is at $\theta \cong 270°$, when its local dynamics are minimally affected by gravity. This angular location of the front is in turn strongly dependent on μ and η, as shown in Fig. 3. The importance of all three independent parameters (ω, μ and η), makes the scaling of the wavelength difficult and probably questionable. Empirically, we find that the λ-curves for different η show similar behaviour when drawn vs. $\omega/\sqrt{\eta}$.

To quantify the response of the front to an impulsive angular acceleration, the following test was performed; the cylinder is accelerated quickly from a straight-front state into a region where strong undulations appear. The adjustment to the final wavelength takes place in less than 10 viscous periods λ^2/ν. The flow adjusts to smaller accelerations more quickly. This is shown in Fig. 12. To avoid transients, the angular velocity was therefore varied slowly.

Figure 13 shows the normalized amplitude β/λ of the undulations for fixed μ and different η; it is a monotonic function of ω. Here the amplitude is twice the usual one, i.e. it is the distance between a crest and a through. For the largest amplitudes the shark-teeth often oscillate axially, causing oscillations in the value of β. In these cases the maximum value of β has been used.

While the mechanism for the axial instability is not completely clear, it seems as though it might be very similar to the mechanism for the fingering instability in the flow down an

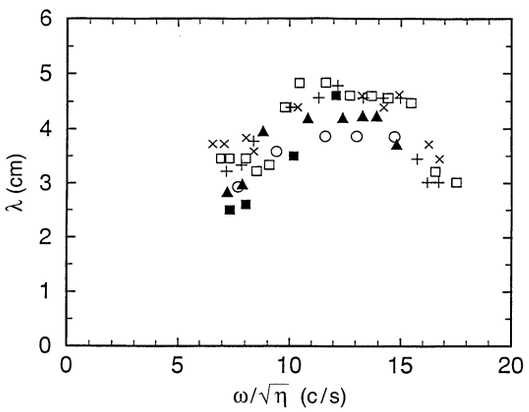

Fig. 11. Wavelength of the shark-teeth vs. $\omega/\sqrt{\eta}$, for $\mu = 24$ cP and, for a few different values of $\eta =$ (■) 2.9%; (○) 3.5%; (▲) 4.5%; (+) 5.0%; (□) 5.5%; (×) 6.5%

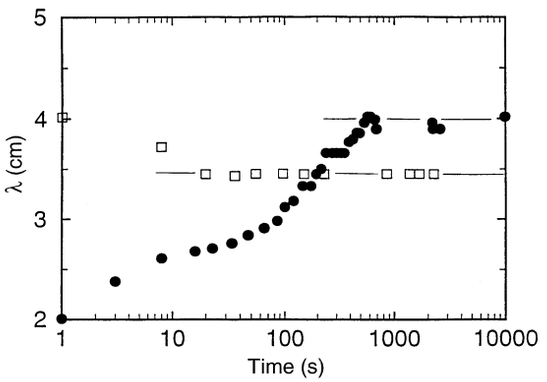

Fig. 12. Changes in the wavelength of shark-teeth with time, after the cylinder has been rapidly accelerated from rest to 2.2 c/s (●). Then after about 3 h the cylinder was accelerated to 2.7 c/s (□). Viscosity is $\mu = 48$ cP and $\eta = 5.5\%$

Fig. 6. Shape of stationary pendant. for $\mu = 8.5$ cP, $\eta = 5.2\%$ and $\omega = 1.1$ c/s. Observe the capillary waves

Fig. 7. Photographs of the thick pendant that remains after the rest of the flow along the cylinder axis has been pulled over into rimming mode, for $\mu = 162$ cP, $\eta = 9.3\%$ and $\omega = 3.3$ c/s. This sideview shows a thick ridge running from it up to the top of the cylinder

Fig. 10. Shark teeth along the entire cylinder, for $\mu = 49$ cP, $\omega = 3.2$ c/s, $\eta = 6.0\%$

Fig. 14a, b. The dimple arrangement relative to each cusp. a Photograph; b sketch of the underlying flow field

Fig. 15. Long-duration transient during the tip-splitting of a single wave as ω is changed. Viscosity is $\mu = 49$ cP, $\omega = 4.4$ c/s, $\eta = 9.1\%$ for cylinder radius of $R = 3.8$ cm and length $L = 59$ cm

Fig. 16. Photograph of the fish-like patterns as the dimples above the cusps have been pulled over the top of the cylinder, leading to a periodic thickening on the top; $\mu = 25$ cP, $\omega = 3.9$ c/s and $\eta = 4.9\%$

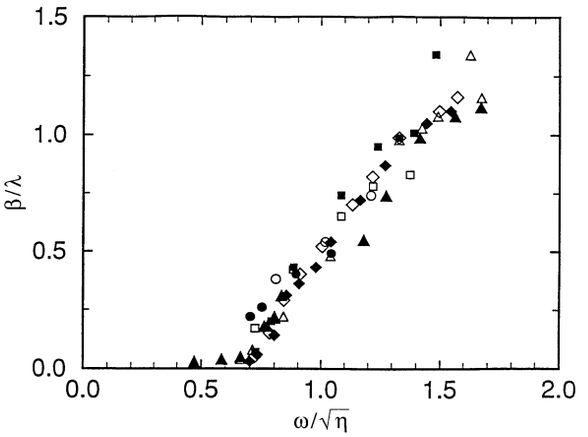

Fig. 13. The amplitude of the shark-teeth β normalized by the wavelength λ, vs. $\omega/\sqrt{\eta}$, for $\mu = 24.5$ cP and various filling fractions; $\eta = (\bigcirc)$ 2.9%; $(\bullet)$ 3.5%; $(\square)$ 4.0%; $(\blacksquare)$ 4.5%; $(\diamond)$ 5.0%; $(\blacklozenge)$ 5.5%; $(\triangle)$ 6.5%; $(\blacktriangle)$ 7.0%

inclined plane (Huppert 1982), Troian et al. (1989), Goodwin and Homsy (1991). In that scenario, the size of the ridge of fluid at the contact line, determined by the capillary number, determines the transverse wavelength of the fingers. Any transverse height perturbations cause a reduced vertical shear and a runaway growth of the finger as first shown by Goodwin and Homsy (1991). This might be modified by the dynamics at the contact line itself as suggested by Bertozzi and Brenner (1996). In our experiment there is a recirculating region at the bottom of the cylinder corresponding to an eddy that sits on the thin fluid film that coats the cylinder. The stagnation point at that leading edge of the recirculating region corresponds to the contact line in the inclined plane flow. Then, as the angular velocity is increased to some critical value, the recirculating region might lose stability to a varicose mode in a manner similar to that in the inclined plane. This idea is currently being studied in the context of a second-order lubrication theory by Hosoi and Mahadevan (1996).

The flow field around the cusps was visualized by seeding fluid with small particles. This revealed two counterrotating vortices which reconnect to the fluid surface on both sides of the cusp. These strong vortical flow close to the front lead to a number of localized bumps and dips (dimples) in the free surface. Some dimples are in phase with the cusps, others develop near the center of each wave as well as at the stagnation point upstream of the cusp; for example, the configuration with 5 dimples is shown in Fig. 14.

The flow field on the rising side of the film associated with the frontal undulations sometimes develop staggered patterns. These shapes often appear to be of a transient nature, appearing when the angular velocity is increased, but usually disappear after long time. They last however for long enough to represent a quasi-stable state. Similarly the shark teeth sometimes develop long-duration transient states, with complicated crest-forms, shown in Fig. 15. For the largest cylinder the crest of the teeth sometimes develop lips reminiscent of the ridge at the contact line for a fluid flowing down an inclined plane (Huppert 1982).

As the dimples get pulled up to $\theta = 0^\circ$ the teeth become unstable and oscillate axially. For moderate η, this leads to a stable fish-like pattern, shown in Fig. 16. Here, the thickness variations of the coating fluid film are clearly visible.

Finally, we mention the robust nature of the cusp-like patterns. They form very quickly when the fluid falls out of rimming flow and forms a new front.

4.4.2 Metastable states

We have observed a stable state consisting of a straight front with only one cusp (see photograph in Thoroddsen and Mahadevan 1996). This state is metastable; depending on initial conditions one can have either an isolated cusp or a straight front. This state was reached by suddenly decreasing the cylinder rotation speed just before the transition to rimming flow and is very robust. It persisted for at least 1200 cylinder rotation periods. This single cusp sometimes exhibited small-amplitude vertical periodic oscillations with a period of about 3 times the cylinder rotation period. In a different metastable state half of the cylinder had a straight front, the other half had shark teeth with cusps. This configuration was observed to change slowly. The cusp adjacent to the straight front would suddenly fall down to the level of the straight front. One cusp would in this manner disappear after about 20 cylinder rotation periods. The straight section would invade the cusped region. These states were not realized if the cylinder was accelerated slowly.

4.4.3 Counter-flowing jets and surface steps

Here we describe the frontal undulations and flow fields inside the pool, which appear for volume fractions larger than those described above for the shark teeth. For large η the flow inside the pool of the cylinder becomes three dimensional very quickly. The recirculating region develops spanwise variations with strong localized counter-flowing jets. This flow can lead to steplike patterns on the pool surface (shown in Fig. 17) as well as smooth undulations of the front. We refer to these surface steps as a duckbills. The counter-flowing jets produce strong vortices inside the pool. The localized vortical motions are at about 45° relative to the cylinder axis and produce the surface duck bills at the center of the pool.

→

Fig. 17. Photograph of the backward-facing steps on the surface of the deep pool

Fig. 19. Travelling wave pattern on the front for the largest cylinder, $R = 14.6$ cm, $\mu = 47$ cP, $\omega = 2.9$ c/s and $\eta = 5.1\%$, with the wavelength $\lambda \approx 2.5$ cm

Fig. 22. **a** Equispaced curtains along the entire span of the cylinder, for $\mu = 120$ cP, $\eta = 18.2\%$, $\omega = 4.9$ c/s; **b** closeup of a partial curtain, for the 59 cm long cylinder, $R = 3.8$ cm, $\mu = 28$ cP, $\eta = 32.7\%$; $\omega = 7.2$ c/s. The average spacing of the curtains along the whole cylinder is 3.3 cm in this case

Fig. 23. Air entrainment and avalanche, traveling along the front. The avalanches are converging from both sides, for $\mu = 144$ cP, $\omega = 3.8$ c/s, $\eta = 14.7\%$. The initial angle of the front was $\theta \approx 260^\circ$ and following the avalanche the front has retreated by about 10°

Fig. 25. Hydroplaning drop being shed out of the bubbly front, for $\mu = 144$ cP, $\eta = 11.6\%$ and $\omega = 3.9$ c/s

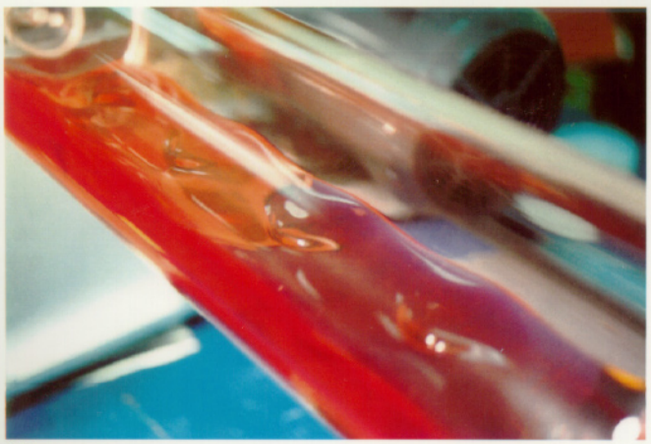

17

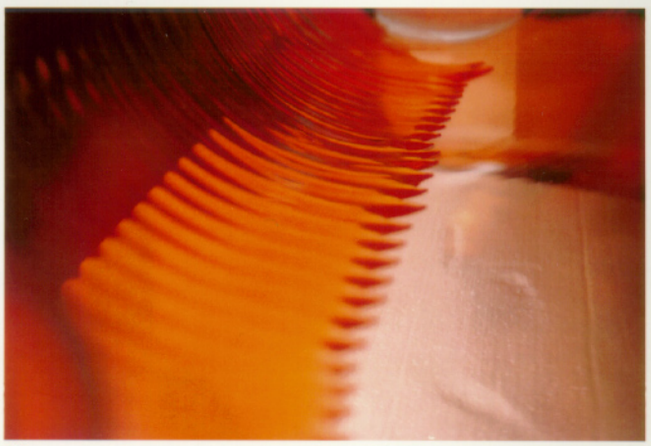

19

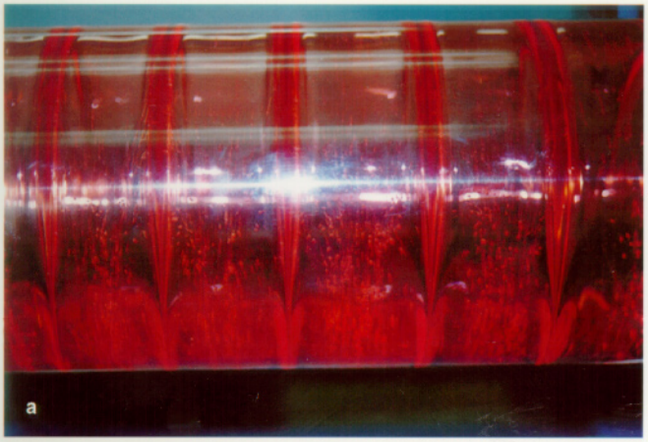

23

22a, b

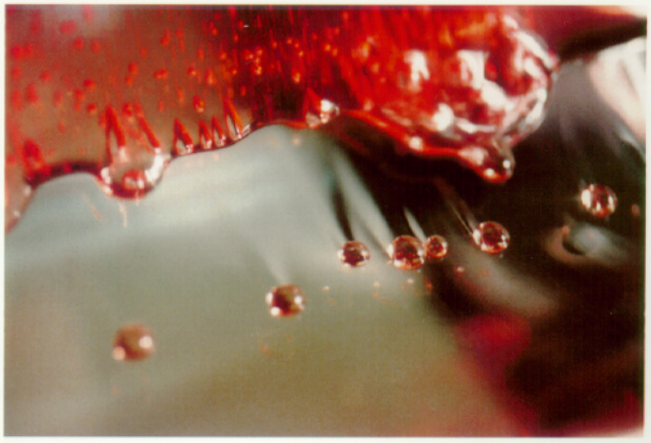

25

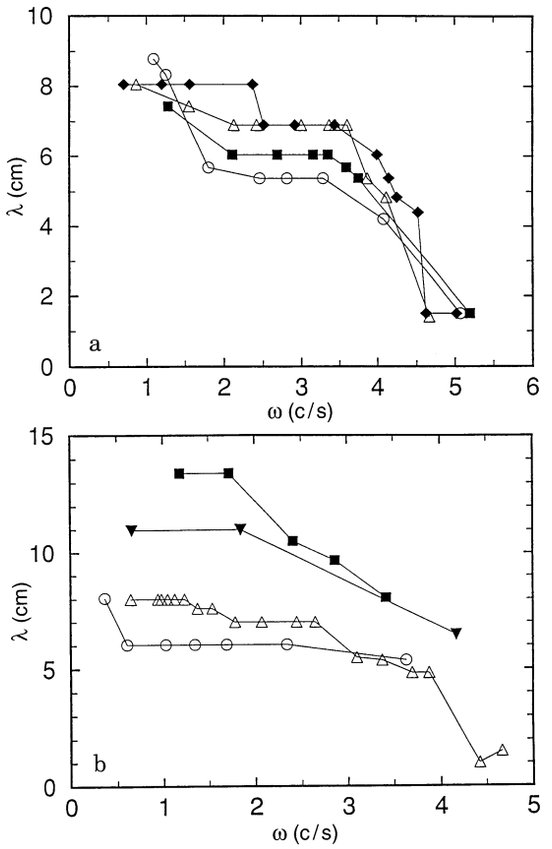

Fig. 18a, b. Wavelength of the frontal undulations associated with the counterflowing jets vs. cylinder rotation rate. **a** for a fixed $\mu = 29$ cP and $\eta = (\bigcirc)$ 8%; (■) 9%; (△) 10% and (◆) 12%; **b** wavelength for a few representative parameters, with the following values of (η, μ). (10%, 17 cP) (○); (9.5%, 24 cP) (△); (17%, 58 cP) (▼); (26%, 165) (■). Note that the wavelength increases with viscosity. The sudden reduction in the wavelength for the open triangles marks the transition into traveling waves

In a different parameter regime (larger η) this deep pool flow generates a pronounced bump on top of each undulation, in phase with the tip of the undulations. Axial oscillations of these large bumps are common.

The wavelength of the frontal undulations associated with the counter-flowing jets is plotted as a function of ω in Fig. 18. Here, in contrast to the wavelength of the shark-teeth which is non-monotonic, the wavelength decreases monotonically with ω. The wavelength is longer at higher viscosities. For the largest ω there is a sudden decrease in λ. This change is associated with a sudden transition from stationary undulations to axial traveling waves, shown in Fig. 19. These waves start at a fixed interior point along the front and can propagate in both directions. The speed of the traveling waves on the front is very small. For $\mu = 26$ cP and $\eta = 9.5\%$ at $\omega = 4.66$ c/s, the axial velocity of the ($\lambda = 1.6$ cm) waves is 2.3 cm/s, while the azimuthal speed of the cylinder $2\pi\omega R$ is 80 times this speed. The traveling waves occur at angular velocities where no significant pool remains at the bottom of the cylinder. Similar sideways-traveling parity-breaking waves have been studied by Pan and deBruyn (1994) for the printer's instability.

4.5
Dimple oscillations

As the angular velocity is increased the surface dimples above the cusps are pulled farther up the rising side of the cylinder. When the dimples approach the vertical ($\theta \approx 0$) the tooth pattern is often observed to become unstable and starts oscillating sideways, sometimes violently. The dimples do also in some cases start oscillating slowly in staggered pairs in the azimuthal direction, with the adjacent dimples being out of phase. These oscillations are coupled to the axial motion of adjacent shark-teeth. Specific parameter values where this phenomena is observed are shown in Fig. 20a.

For a limited range of parameters, where the cusps sit close to the bottom of the cylinder, the dimple regions above the shark-teeth cusps start popping, in what looks like the surface rising and falling very suddenly in a localized spot. This instability is accompanied by slight axial motions of the two adjacent shark teeth, which translates the cusp slightly in the θ direction. This popping occurs in a very narrow range of parameters, shown in Fig. 20a. The popping occurs locally, but often travels along the axis from cusp to cusp, in what appears to be a quasi-periodic manner.

The popping described above is a temporally discrete phenomena, with the fluid surface remaining calm, until it suddenly rises in a burst at a localized spot above the cusp,

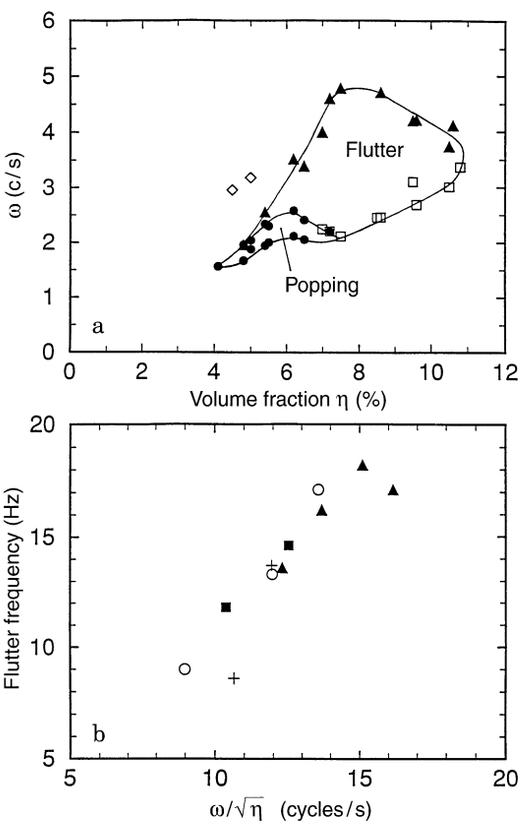

Fig. 20. a Range of parameters where dimple popping and flutter is observed, for $\mu = 29$ cP. The diamond symbols identify parameter values where the staggered dimples oscillate azimuthally; **b** frequency of the flutter for different rotation rates and volume fractions η of (■) 6.5%; (○) 7%; (▲) 7.5% and (+) 8.5%

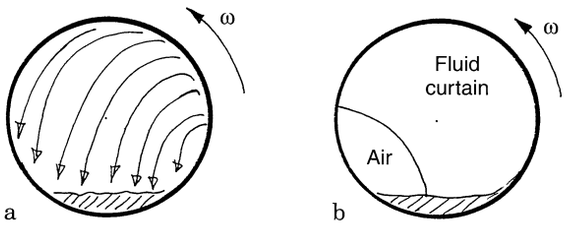

Fig. 21a, b. Curtains spanning the cross-section of the cylinder. **a** Schematic of the pathlines inside the curtains; **b** partial curtains

whereas flutter refers to a continuous high frequency motion, which is clearly visible in the video sequences from light reflected from the fluid surface. Flutter occurs for higher rotation rates, over a large region further above the cusps. It usually occurs above every cusp along the entire cylinder. This flutter occurs for a wide range of ω and is often intermittent in time. It is therefore very unlikely that the flutter is caused by resonance with slight vibrations in the cylinder driving mechanism, but is instead induced by flow inside the coating film.

The fluttering frequency was determined from slow-motion playback of the video frames and is shown in Fig. 20b. The flutter frequency grows with the effective angular velocity of the cylinder.

The popping and flutter of the regions above the cusps may be connected to the dynamics of the vortices in the fluid pool. The large sensitivity of the cusped front feeds disturbances down-stream, which affect the stagnation point under the downstream dimple.

4.6
Fluid curtains

The combination of high volume fractions and large viscosity leads to the formation of radial sheets of fluid that span the whole cross-section and partitions the cylinder, see Figs. 21 and 22. These sheets were called hygrocysts by Balmer (1970). Balmer's observations were limited to much larger volume fractions ($\eta > 40\%$) than are studied here. The formation of these walls or curtains is often triggered at the ends, leading to the concurrent formation of two such curtains, one at each end. At higher ω, additional curtains are formed until the entire cylinder has been filled with them. The curtains have approximately equal spanwise spacing. The flow inside the curtains was studied by seeding the fluid with particles and is approximately sketched in Fig. 21. The spacing of the curtains was briefly studied and was found to be fairly independent of μ. In some cases the curtains only span a limited fraction of the cylinder length as each curtain suspends a considerable amount of the total fluid.

The formation of the curtains is usually preceeded by thickening of a fluid ridge over the top of the cylinder, as shown in Fig. 7; and is independent of whether or not the coating fluid film has air entrained in it.

The lower half of the curtains sometimes exhibits large axial oscillations of the size of $\frac{1}{2}\lambda$ without breaking.

Partial curtains can exist at rotation rates slightly lower than the full curtains, see Fig. 22b. The partial curtains were sometimes realized simultaneously along the entire span of the cylinder. The flow field and the shape of the edge where the partial curtain separates from the coating fluid film is particularly intricate, due to the presence of a stagnation point on the free surface of the fluid sheet on the cylinder.

4.7
Air-entrainment and frontal avalanches

For certain parameter values and relatively large η, air is entrained at the front. Figure 23 shows such an event and demonstrates how the air entrainment changes the front. In this case the front was initially at $\theta \approx 260^\circ$. As the air gets entrained the front falls backwards, by about 10° (to $\theta \approx 250^\circ$), under gravity in a sudden avalanche. This is due to the reduction in the effective viscosity of the bubbly sheet. Note the presence of bubbles inside the sheet, in Fig. 23, only in the part of the front where the avalanche has advanced. The avalanche is usually initiated at one or two places and then travels axially along the front. The air entrainment fan is at an angle of around 45° to the axis and travels sideways at about 20 cm/s for the case shown in Fig. 23.

In the presence of shark-teeth the entrained bubbles tend to collect at the cusps, forming large bubbles, which pop periodically.

Figure 24 shows the angular location of the straight front where air starts being entrained, for different η and μ. The entrainment depends strongly on η, but appears to be fairly independent of μ. This is a surprising result, since it suggests that the viscous forces in the fluid under the front do not affect the entrainment directly. For lower values of μ it requires larger ω to pull the front to a certain angular location, as shown in Fig. 3. The entrainment mechanism appears to be dictated by surface tension and gravity and η determines the thickness of the recirculating region above the front. The conditions and mechanism of this air entrainment is of great practical importance and deserves further study.

4.8
Hydroplaning drops

When air is entrained under the front the shedding of drops from the front can occur. This happens when the front is far enough up on the rising side of the cylinder so that when the front entrains air fluid drops separate from it. These drops hydroplane on the fluid sheet. Figure 25 shows drops being shed from an irregular bubbly front. The drops move along the film like particles and often collide with each other without coalescing.

The entrained bubbles grow and form stretched cusped forms in the areas where the front breaks. The various shapes of bubble-cusps in a different context have recently been studied by Liu et al. (1995).

When the air entrainment occurs on the receding side, i.e. when the front is at $\theta < 260^\circ$, the avalanche does not separate from the front, due to the relative direction of gravity. In this case the pool and fluid sheet have a large number of bubbles, which collect at the cusps of the front and burst when they become sufficiently large.

As the front enters the centrifugal mode, drops are often created from the fluid sheet, forming hydroplaning drops at the

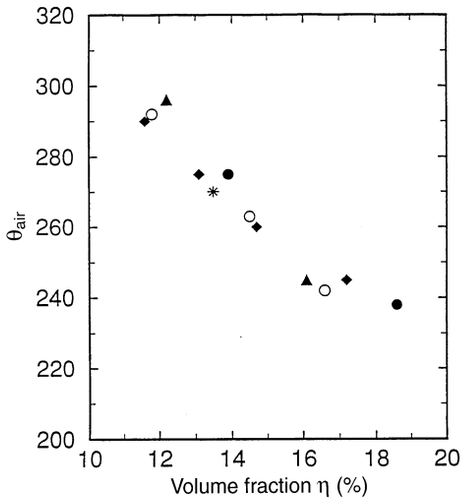

Fig. 24. The angular location θ_{air} of the front where air entrainment begins vs. η, for different viscosities; $\mu = 130$ (○); 144 cP (◆); 154 (★); 196 (△); 230 (●)

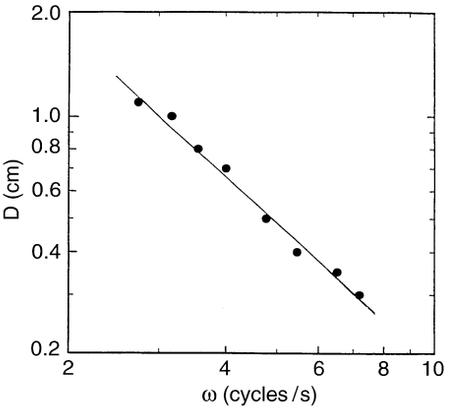

Fig. 26. Axial diameter of hydroplaning drops vs. cylinder rotation rate, for $\mu = 230$ cP and $\eta = 13.7\%$. The best fit line has a slope of −1.4

bottom of the cylinder, while the rest of the fluid is in rimming mode. The larger drops are more prolate and sessile. The drops oscillate back and forth for a while, before settling close to the bottom of the cylinder. The formation and initial size of these drops is different from run to run due to their random creation. However, once they form, their dynamics show interesting and repeatable behavior. The presence of a number of drops, which in many cases slide slowly spanwise, leads to collisions, usually without coalescence. As ω is increased the drops get pulled farther up the rising sheet, leaving a prominent wake on the coating fluid film seen behind the drops in Fig. 25. As ω is increased the drops suddenly shed some of their mass, which gets absorbed in a burst into the underlying fluid sheet. As ω is increased further this process is repeated and the drops become smaller. Figure 26 shows the drop size characterized by the axial drop diameter D as a function of ω for a typical drop. The best fit line on the graph shows a power-law dependence with an exponent of $D \approx \omega^{-1.4}$.

If ω is decreased smaller drops do in some cases coalesce, on colliding. Smaller drops are occasionally observed in the wake of larger drops and are higher along the rising side of the cylinder.

The rotating drop is unstable above a certain rotation speed and centrifugal forces expel a part of the fluid. Seeded particles from the fluid film caught inside these drops show internal rotation, but the tangential velocity due to this rotation rate is much smaller than the corresponding translational speed of the underlying support. A thin layer of air lubricates these drops and the viscous forces generated in this layer force the drop to spin.

The persistence of these drops at much higher rotation rates than is required for the onset of the rimming mode, may present problems in manufacturing using rotomolding (Johnson 1990).

4.9
Rimming flow and hysteresis

For a large enough rotation rate centrifugal forces dominate over gravity and the fluid forms a film that coats the cylinder

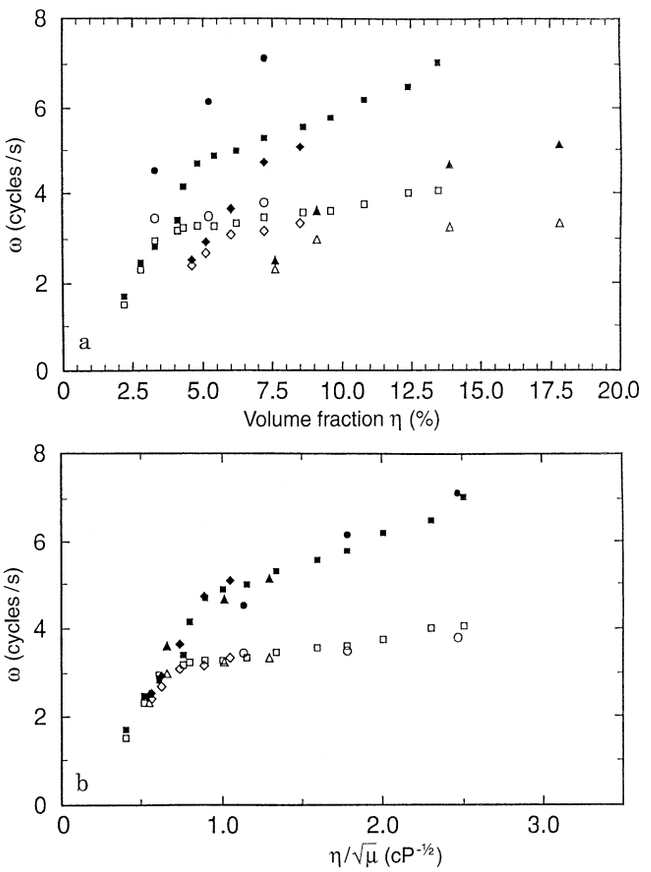

Fig. 27a, b. Hysteresis in the transition to centrifugal mode. Solid symbols indicate transition when ω is increased, whereas open symbols when ω is decreased, for $\mu = 8.5$ (○); 29 (□); 66 (◇); 189 (△) **a** vs. volume filling fraction, η; **b** vs. $\eta/\sqrt{\mu}$

almost uniformly in a rimming mode. The transition to this mode does not scale with η, as shown in Fig. 27. This is especially true for the regimes where the shark teeth are present.

Melo (1993) studied the reverse process, first accelerating all the fluid into the centrifugal mode and then slowly reducing the rotation rate. This gives results that scale very well with his dimensionless parameter. He noticed no hysteresis, but focused on lower Reynolds numbers.

After all of the fluid has entered into rimming flow, one can reduce ω significantly below the value at which the rimming transition occured, before the fluid falls out of that mode and reforms a front. The transition from the centrifugal mode to the front dominated region, is weakly dependent on η and μ, showing only a slight rise with η (see open symbols in Fig. 27). In Fig. 27(b) this data is scaled with $\eta/\sqrt{\mu}$. We observe that the data from a wide range of viscosities collapse onto a single curve and also that there is a specific value of $\eta/\sqrt{\mu}$ below which no hysteresis is observed. The instability of the centrifugally dominated mode is preceded by periodic thickening of the film on the top of the cylinder. These initial axial instabilities do not grow as in the conventional Rayleigh–Taylor instability because of the fluctuating direction of gravity as observed in a rotating frame. Phillips (1960) and Greenspan (1976) have studied these instabilities theoretically.

The arguments put forth below show that for $\eta < \eta_c$, there should not exist any hysteresis. This is dramatically brought out by the data. This critical dimensional effective volume fraction is $\eta_c/\sqrt{\mu} \approx 0.7\ \mathrm{cP}^{-1/2}$.

To study the presence of the hysteresis demonstrated in the transition into and out of rimming flow, we consider the balance of the various forces acting upon a small parcel of fluid, which is just about to be pulled over the vertical on the rising side of the cylinder, where $\theta = 0$ in Fig. 1a. The viscous, gravitational and inertial forces acting on the parcel are given by

$$F_{\text{viscous}} = \mu \frac{\omega R}{h} \ell R \, \mathrm{d}\theta \tag{4.1}$$

$$F_{\text{gravity}} = \rho g h \ell R \, \mathrm{d}\theta \tag{4.2}$$

$$F_{\text{centrifugal}} = \rho \omega^2 R h \ell R \, \mathrm{d}\theta \tag{4.3}$$

Here h is the film thickness at $\theta = 0^\circ$. The transition into the rimming mode is dominated by a balance between gravity and viscous forces, whereas the transition out of the rimming mode is characterized by a balance between gravity and centrifugal forces. From Eqs. (4.1) and (4.2), we get

$$v(\omega R/gh^2) = 1 \tag{4.4}$$

Since $\eta \sim h/R$, this implies that $\eta^2/\mu \sim \omega$, for a fixed R, while Eqs. (4.2) and (4.3) yield

$$g/\omega^2 R = 1 \tag{4.5}$$

This implies that the fluid falls out of the rimming mode at a value of ω that is independent of the film thickness h. The angular velocities for the onset and breakdown of rimming flow using above scaling arguments are different in general. However there is a critical film thickness (or η) for which they are the same. By equating Eqs. (4.4) and (4.5) this yields some $\eta/\sqrt{\mu} = \text{Const.}$ below which there is no hysteresis as shown in Fig. 27b.

References

Balmer RT (1970) The Hygrocyst – a stability phenomenon in continuum mechanics. Nature 227: 600–601

Benjamin B (1957) Wave formation in laminar flow down an inclined plane. J Fluid Mech 2: 554

Benjamin TB; Pritchard WG; Tavener SJ (1995) Steady and unsteady flows of a highly viscous liquid inside a rotating horizontal cylinder. Preprint

Benkreira H; Patel R; Edwards MF; Wilkinson WL (1994) Classification and analysis of coating flows. J Non-Newtonian Fluid Mech 54: 437–447

Bertozzi A; Brenner M (1996) personal communication

De Bruyn RJ; Pan L (1995) Delayed onset of ribbing instability due to finite-size effects. Phy Fluids 7: 2185–2190

Goodwin R; Homsy GM (1991) Viscous flow down a slope in the vicinity of a contact line. Phys Fluids 3: 515–528

Goodwin R; Tavener S (1996) personal communication

Greenspan HP (1976) On a rotational flow disturbed by gravity. J Fluid Mech 74: 335–351

Huppert HE (1982) Flow and instability of a viscous current down a slope Nature 300: 427–429

Johnson RE (1988) Steady-state coating flows inside a rotating horizontal cylinder. J Fluid Mech 190–321

Johnson RE (1990) Coating flow stability in rotational molding. Engineering Science, Fluid Dynamics (Ed. George W. Yates) Singapore: World Science Publishing, pp. 435–449

Kapitza PL; Kapitsa SP (1949) J Exptl Theor Phys USSR 19: 105

Karweit MJ; Corrsin S (1975) Observations of cellular patterns in a partially filled, horizontal cylinder. Phys Fluids 18: 111–112

Kovac JP; Balmer RT (1980) Experimental studies of external hygrocysts. J Fluids Eng. Transactions of the ASME 102: 226–230

Liu YJ; Liao TY; Joseph DD (1995) A two-dimensional cusp at the trailing edge of an air bubble rising in a viscoelastic liquid. J Fluid Mech 304: 321–342

Lin YY (1986) Numerical solutions for flow in a partially filled, rotating cylinder. SIAM J Sci Stat Comput 7: 560

Hosoi AE; Mahadevan L (1996) Axial instability of coating flow in a horizontal rotating cylinder. In preparation

Melo F (1993) Localized states in a film-dragging experiment. Phys Rev E 48: 2704–2712

Melo F; Daoudy S (1993) From solitary waves to static patterns via spatiotemporal intermittency. Phys Rev Lett 71: 3283

Moffatt HK (1977) Behavious of a viscous film on the outer surface of a rotating cylinder. J Mecanique 16: 651

Orr FM; Scriven LE (1978) Rimming flow: numerical simulation of steady, viscous, free-surface flow with surface tension. J Fluid Mech 84: 145

Pan L; DeBruyn JR (1994) Spatially uniform traveling cellular patterns at a driven interface. Phys Rev E 49: 483–493

Pearson JRA (1960) The instability of uniform viscous flow under rollers and spreaders. J Fluid Mech 7: 481–500

Preziosi L; Joseph DD (1988) The run-off condition for coating and rimming flows. J Fluid Mech 187: 99–113

Phillips OM (1960) Centrifugal waves. J Fluid Mech 7: 340

Rabaud M; Couder Y; Michalland S (1991) Wavelength selection and transients in the one-dimensional array of cells of the printer instability. Eur J Mech B-Fluids, V10 N2: 253–260

Rabaud M (1994) Interface dynamics in the printer instability. Ann de Phys, 19: 659–690. Language: French

Ruschak KJ; Scriven LE (1976) Rimming flow of liquid in a rotating horizontal cylinder. J Fluid Mech 76: 113–127

Troian SM; Herbolzheimer E; Safran SA; Joanny JF (1989) Fingering instabilities of driven spreading films. Europhys Lett, 10: 25–30

Thoroddsen ST; Mahadevan L (1996) Shark-teeth pattern in coating flow inside a horizontally rotating cylinder. Phys Fluids 8: S10

Vallette DP; Edwards WS; Gollub JP (1994) Transition to spatio-temporal chaos via spatially subharmonic oscillation of a periodic front. Phys Rev 49: R4783–4786

Zhang HB (1995) Selected topics in viscous flow: Coating flow with rotation. PhD Dissertation, University of Illinois at Urbana-Champaign